# Spatially extended charge density wave switching by nanoscale local manipulation in a VTe 2 monolayer

Ulysse Chazarin, Mahé Lezoualc'h, Abhishek Karn, Jyh-Ping Chou, Woei Wu Pai, Cyril Chacon, Yann Girard, Vincent Repain, Amandine Bellec, Sylvie Rousset, et al.

# Spatially extended charge density wave switching by nanoscale local manipulation in a $VTe_2$ monolayer

U. Chazarin,[†,‡] M. Lezoualc'h,[¶] A. Karn,[‡] J.P. Chou,[§] Woei Wu Pai,[*,‡] C. Chacon,[†] Y. Girard,[†] V. Repain,[†] A. Bellec,[†] S. Rousset,[†] C. González,[‖,⊥] A. Smogunov,[¶] J. Lagoute,[*,†] and Y. J. Dappe[¶]

†*Université Paris Cité, Laboratoire Matériaux et Phénomènes Quantiques, CNRS, F-75013, Paris, France*

‡*Center for Condensed Matter Science (CCMS), National Taiwan University, 11106 Taipei, Taiwan, ROC*

¶*SPEC, CEA, CNRS, Université Paris-Saclay, CEA Saclay, 91191 Gif-sur-Yvette Cedex, France*

§*Department of Physics, National Changhua University of Education, 50007 Chuanghua City, Taiwan, ROC*

‖*Departamento de Física de Materiales, Universidad Complutense de Madrid, E-28040 Madrid, Spain*

⊥*Instituto de Magnetismo Aplicado UCM-ADIF, Vía de Servicio A-6, 900, E-28232 Las Rozas de Madrid, Spain*

E-mail: Corresponding_author:wpai@ntu.edu.tw; jerome.lagoute@univ-paris-diderot.fr

**Abstract**

Monolayer transition metal dichalcogenide $VTe_2$ exhibits multiple charge density wave (CDW) phases, mainly $(4 \times 4)$ and $(4 \times 1)$. Here we report a facile dynamic and tens-of-nanometer scale switching between these CDW phases with gentle bias pulses in scanning tunneling microscopy (STM). Purposely bias pulses stimulate reversible random CDW symmetry change between the isotropic $(4 \times 4)$ and anisotropic $(4 \times 1)$ CDWs, as well as CDW phase slips and rotation. The switching threshold of ∼1.0 V is bias-polarity independent and the switching rate varies linearly with the tunneling current. Density Functional Theory (DFT) calculations indicate a coherent CDW phase switching incurs an energy barrier of ∼2.0-3.0 eV per $(4 \times 4)$ unit cell. While being a challenge in understanding the observed large-area CDW random fluttering, we provide some possible explanations. The ability of manipulating electronic CDW phases sheds new lights on tailoring CDW properties on demand.

## Keywords

Scanning Tunneling Microscope, Density Functional Theory, Transition Metal Dichalcogenides, $VTe_2$ monolayer, Charge Density Wave

Layered transition metal dichalcogenides (TMD) host a plethora of exotic ground states such as Superconductivity, Mott Insulator or Charge Density Wave (CDW). Unlike the one-dimensional case of CDWs, a typical manifestation of Peierls distortion, understanding the origin of CDWs in 2D and 3D materials is compounded by other mechanisms such as q-dependent electron-phonon coupling or excitonic CDW.[1] In cases of coexisting multiple CDW states in a material,[2] it is less studied if switching between these CDWs can be manipulated or controlled. 1T-$VTe_2$ monolayer is a case in which multiple CDW phases coexist. Monolayer (ML) $VTe_2$ undergoes a structural transition of its 1T phase at $\approx$ 135 K,[3] and concomitantly a CDW of periodicity 4a (a: lattice spacing) occurs. The 4a periodicity corroborates with the

calculated phonon softening in ML $VTe_2$ phonon spectra (see supporting information Fig. S1). Experimentally, a $(4 \times 4)$ CDW in 1T-$VTe_2$ monolayer has been reported by Y. Wang *et al.* using low-energy electron diffraction and angle-resolved photo-emission spectroscopy.[4] This CDW phase was also reported in scanning tunneling microscopy (STM) experiments.[5–7] The $(4 \times 4)$ phase was also found to coexist with a $(4 \times 1)$ phase[8–10] or with a $2\sqrt{3} \times 2\sqrt{3}$ phase.[8,11] A $(5 \times 1)$ phase has also been reported by M. Liu *et al.*[8] The $(4 \times 1)$ phase has been attributed to strain[8] or defects.[9] The exact origin of the different phases is still to be understood. A theoretical calculation shown in the supplementary information hints that $(4 \times 1)$ and $(2\sqrt{3} \times 2\sqrt{3})$ phases are linked to two different soft phonon modes (Fig. S1).

The CDWs coexistence suggests that the two observed CDWs are close in energy. It is thus of interest to understand the competition between these two phases and the control of CDW by external perturbations. This opens a route to selectively enhance a CDW phase in such systems. For example, the "David-star" CDW phase of 1T-$TaS_2$ can be driven into a "hidden" chiral enantiomer CDW phase with light pulses[12] and monolayer 1T-$NbSe_2$ CDW chirality switching by STM pulses was reported.[13] In bulk $NbSe_2$, several CDW state switchings were achieved using STM.[14] In general, the CDW switching mechanisms are vague. Here, we present a study of tuning CDW phases of a $VTe_2$ monolayer. Unlike previous works[13,14] where the CDW switching conditions generally involve a pulse threshold from 5 to 10 V, the CDW switching of ML $VTe_2$ is initiated with a low perturbation threshold (around 1 V, 100 pA). Moreover, here we have observed all the possible CDW switchings in our system, *i.e.* transitions between $(4 \times 4)$ and $(4 \times 1)$ CDWs, and rotation and phase slips of the $(4 \times 1)$ CDW.

The $VTe_2$ monolayer grown on graphene bilayer on SiC(0001) exhibits multiple CDW domains (Fig. 1.a). Two phases, (4×4) and (4×1), are present simultaneously (see supporting information Fig. S7). The (4×4) phase exhibits a six-fold symmetry and a periodicity of 1.45 nm (4 times the experimental lattice constant 0.36 nm) (Fig. 1.b). The (4×1) phase

has an anisotropic lineshape ridge pattern with a periodicity of 1.45 nm normal to the ridges and 0.36 nm along the ridges (Fig. 1.c). This (4×1) CDW phase can take three different directions corresponding to the three close-packed directions of the $VTe_2$ layer. In our sample, the CDW domain average size is approximately 10 nm or more. The local density of states (LDOS) probed by $dI/dV$ scanning tunneling spectroscopy (STS) exhibits the expected features of typical group V based TMDs[15] with slight differences between (4×4) and (4×1) phases (see supporting information Fig. S8).

In typical STM images, some areas appear noisy (Fig.2.a). Such noise reflects the dynamics occurring at the surface.[16] Here it is a fingerprint of the CDW phase switching. The time evolution of the tunneling current at such areas reveals a clear two-level telegraph signal (Fig.2.b), indicating that the CDW is switching between 2 phases.

When the tunneling parameters are optimized to stabilize the CDW phases during the scanning, each phase can be visualized. The CDW phase switching can be induced by a voltage pulse with the STM tip after acquisition of a stable image, which allows to visualize the two phases. Figure2.c shows a sequence of images obtained in non-perturbative conditions with a voltage pulse of 0.7 V applied in between at the blue cross location. In this sequence, the central part switches from (4×1) (Fig.2.c top) to (4×4) (Fig.2.c middle), and switches back to (4×1) (Fig.2.c bottom). The surrounding domains, (4×1) on the left and (4×4) on the right remain unaffected. This shows that the CDW domains can be switched reversibly between the two CDW phases.

To investigate the switching mechanism, we analyzed the tunneling current as a function of time. Figure 2.b shows the tunneling current recorded with an applied bias voltage of 0.9 V at the location of the red cross in Fig.2.a with the feedback loop turned off. The high current level (196±0.5 pA) corresponds to the (4×1) CDW and the low level (175±0.5 pA) corresponds to the (4×4) phase. This is because, as seen in the topographic image, the tip is on the bright maximum of the CDW in the (4×1) phase. The experimental signal is

fitted by an ideal telegraph signal.[17] From this fit, we extract the mean yield of the process, representing the number of switches per electron given by $\eta_\alpha = \frac{1.6\times10^{-7}}{I_\alpha T_\alpha}$. Here, $I_\alpha$ is the tunneling current intensity in pA associated to the level $\alpha$, $T_\alpha$ the average time spend in the level $\alpha$, and $\eta_\alpha$ is the average number of switchings triggered by one electron in the level $\alpha$. In Fig.2.b, the mean yield is $6.3 \times 10^{-9}$ for the high current level, and $1.1 \times 10^{-9}$ for the low current level. In Fig.2.d, we show the mean yield as a function of the bias voltage for the low (black) and high (red) current levels. For each measure, the tip was located at the same position (red cross in Fig.2.a), and the high current level was fixed at 200 pA. Below 0.7 V, the number of switches per electrons drops sharply but seems to stabilize at high voltage. The plot is nearly symmetric with respect to the zero bias and reveals a threshold at positive and negative polarity around 1 V. The threshold biases do not correspond to any LDOS peaks (see supporting information Fig. S8) of ML $VTe_2$ suggesting that the CDW switching is not caused by resonances, but more likely related to inelastic electron tunneling processes. Furthermore, the variation of the yield in Fig. 2.e shows no clear monotonic trend with the current, indicating that there is no significant correlation between current and yield. This points toward a one-electron process.

A tip pulse can also induce a switching between different rotational orientations. In Fig.3a-c the area marked by a blue circle is first switched from (4×4) to (4×1) (Fig.3a,b), and then rotated by 60 degrees from $(4\times1)_\alpha$ to $(4\times1)_\beta$ (Fig.3b,c). In addition, the phase of the (4×1) CDW with respect to the atomic lattice can adopt different possible values. As observed in Fig.3d-f, the application of a voltage pulse can induce a shift of a CDW domain and thus a CDW "phase slip". By applying a voltage pulse during the scanning, a discontinuity of the (4×1) CDW is seen in Fig.3d corresponding to a shift of the CDW by one atomic lattice distance ($\pi/2$ phase shift) (Fig.3e,f).

As can be seen in Fig.3, the CDW domain size can change upon tip excitation indicating

that the local excitation can induce a simultaneous change of adjacent domains. In Fig.3c, the circled area is part of a very large domain in the $(4\times1)_\beta$ phase, but in Fig.3b the circled area is part of a much smaller domain. Interestingly, after successive switches, the area comes back to its initial state. This proves that the switching of the CDW between different orientations or translations is reversible (see supporting information Fig. S9) and is not related to the formation of defects during tip pulse, otherwise random and irreversible CDW deformations would occur.

For a deeper understanding of the CDWs and their switching we have performed Density Functional Theory (DFT) calculations.

A CDW structure is determined and characterized by a phonon mode with imaginary frequency for a specific wavevector $\mathbf{q}$ in the $1^{st}$ Brillouin zone. This wavevector in the reciprocal space determines the periodicity of the CDW, *e.g.* (4×1), in real space. Therefore, we have first calculated the harmonic phonon dispersion along the high-symmetry points of the $1^{st}$ Brillouin zone, from a fully DFT-optimized 1T-$VTe_2$ (1×1) unit cell. This dispersion, which corresponds to the eigenvalues of the dynamical matrix, is shown in the Supporting information (Fig. S1). We obtain a phonon with imaginary frequency at a reciprocal vector corresponding to a (4×1) modulation. For symmetry reasons, this phonon is 6-fold degenerated in the $1^{st}$ Brillouin zone, leading to the 3 different $\alpha$, $\beta$ and $\gamma$-(4×1) CDW domains observed experimentally. Note that the combination of at least two of these modes leads to the (4×4) CDW phase. From the diagonalization of the dynamical matrix, we also obtain the eigenvectors of these different phonon modes. These normalized eigenvectors correspond to the atomic displacements directions (polarization vectors)[18] of each phonon mode with respect to the atomic positions in the pristine 1T-$VTe_2$ unit cell (1×1). Hence, to obtain the three (4×1) domains and the (4×4) atomic structures, we generated the atomic displacements $\mathbf{\Delta u_{n_1,n_2}}$ in a (4×4) unit cell according to $\mathbf{\Delta u_{n_1,n_2}} = \sum_{j=1}^{2} \mathbf{X_j} e^{\mathbf{q_j}\cdot(n_1.\mathbf{a_1}+n_2.\mathbf{a_2})}$, where $n_1$ and $n_2$ label the cells in the lattice, $\mathbf{q_j}$ is the reciprocal lattice vector of the eigenvector

phonon mode $\mathbf{X_j}$ and $\mathbf{a_1}$ and $\mathbf{a_2}$ are the lattice vectors. While each (4×1) domain corresponds to one phonon mode, the (4×4) phase corresponds to the superposition of at least two (4×1) domains. Therefore the (4×4) atomic structures is built from the sum of the atomic displacements generation of two (4×1) modes. Since the eigenvectors of the dynamical matrix are normalized, the exact amplitude of the atomic displacements with respect to their equilibrium positions are not known. Consequently, we set the atomic displacements with respect to the equilibrium position to be about $2-5\%$ of the lattice constant $a$, as an initial tryout CDW amplitude before performing a full optimization of the different structures. After optimization, the net atomic displacement with respect to the equilbrium position in the pristine phase rather lies between $2-10\%$, which in average corresponds to an atomic displacement of 20 pm. The obtained energy gain between these different CDW superstructures and the pristine structure is about 30 meV per unit cell.

Turning to rotation and translation, we label $(4\times1)_\gamma$ our initial (4×1) structure, in agreement with the experimental STM images. From this structure, we have performed a 60° rotation and an atomic lattice constant translation, in order to reproduce respectively the $(4\times1)_\alpha$ and the shifted $(4\times1)_\gamma$ forms of the CDW. The structures are shown in Supporting information (Fig.S2). For an accurate visualization of the different structures, we have performed STM simulations following the formalism explained in reference[19] (see supporting information for further details).

The calculated STM images are shown in Fig. 4. They are in good agreement with experimental results, with lineshape features of different orientations for the (4×1) phase ($(4\times1)_\gamma$ and $(4\times1)_\alpha$) and a hexagonal symmetry for the (4×4) phase. Also the $(4\times1)_\gamma$ shift CDW clearly corresponds to a lateral shift of the $(4\times1)_\gamma$. To shed some light on the transition mechanisms, we have performed Nudged Elastic Band (NEB)[20] calculations as implemented in the Fireball code.

This method determines the atomic motion of smallest energy to move from an initial to

a final configuration. The evolution of the energy along the atomic motion (*i.e.* following the set of configurations) gives an estimation of the potential energy barrier to switch from the initial to the final configuration. Here we have applied this methodology to estimate the potential energy barrier of transition between the $(4\times1)_\gamma$ and the (4×4), the $(4\times1)_\gamma$ and the $(4\times1)_\alpha$ (CDW rotation) and the $(4\times1)_\gamma$ and the $(4\times1)_\gamma$ shift (one atomic row CDW shift) CDWs. For all the calculations, we have used three intermediate configurations between the initial and final states, a force tolerance of 0.05 eV/Å, and a spring strength of 0.1 eV/Å$^2$. Note that the value of the spring strength must be not too small, in particular if the potential energy surface is complicated, and not too large, leading to a less precise estimation of the energy profile. The calculated energy profiles are shown in Fig. 4. For each energy profile, the intermediate atomic configurations determined within the NEB calculation are represented in Figure S3, S4 and S5 in the Supplementary information. We can observe potential energy barrier of $\sim$ of 3.0 - 3.3 eV per (4×4) unit cell for the $(4\times1)_\gamma \rightarrow$ (4×4) and $(4\times1)_\gamma \rightarrow (4\times1)_\gamma$ shift transitions, and of about 1.7 eV per (4×4) unit cell for the $(4\times1)_\gamma \rightarrow (4\times1)_\alpha$ rotation. Therefore we can deduce that the easiest transition corresponds to the rotation of a (4×1) domain. This can be understood by the number of components of each CDW phase. Indeed, a (4×1) phase corresponds to a lattice distortion along a single axis, as observed in the experimental STM images ($\alpha$, $\beta$ or $\gamma$), whereas the (4×4) phase corresponds to a linear combination of lattice distortions along at least two axes. Hence, we can infer that the energetic cost to transit from a one-axis to a two-axes distortion is higher than to only rotate a single-axis distortion. Despite the higher energetic cost of the (4×1) $\pi/2$ shift of one atomic row (which might arise from standard DFT overestimation), the result is qualitatively consistent with our experiments, confirming the general trend that the CDW $\pi/2$-phase shift requires a stronger pulse (see fig. 3d). Further experimental investigation is needed for a more quantitative experimental comparison of the energy barriers of the switching processes. We have also performed similar calculations with charged $VTe_2$ monolayers

in order to explore its possible effects on the potential barriers. The effect is minor without any significant change on the barriers. This theoretical analysis supports the experimental hypothesis that the CDW switching is induced by inelastic electron tunneling processes and not by an electrostatic or field effect. Furthermore, we have performed test calculations where one atom or one atomic row is initially displaced in the initial structure before the NEB calculation, to see if it helps in reducing the potential energy barrier. Unfortunately these calculations have resulted to be unsuccessful, which in the end, is in agreement with the high energetic cost obtained to shift a $(4\times1)_\gamma$ CDW of one atomic row.

From the calculations it appears rather unlikely that a single tunneling electron can transfer enough energy to switch a CDW nano domain with a size of 10 nm or more ($\sim$50 (4×4) CDW unit cells, leading to a total energy barrier of $\sim$100 eV or more). We surmise on a resolution to this seemly conflict. The CDW switching could be incoherent or coherent. In an incoherent process, a single $VTe_2$ unit cell (1/16 of the CDW unit cell size) is switched and then propagates. The switching energetic cost would be 106 meV for the $(4\times1)_\gamma \rightarrow (4\times1)_\alpha$ rotation, and $\sim$188-206 meV for the $(4\times1)_\gamma \rightarrow (4\times1)_\alpha$ and $(4\times1)_\gamma \rightarrow (4\times1)_\gamma$ $\pi/2$-shift transitions. During the process, an energy compensation mechanism is required to keep the "domino-like" CDW switching going. This may be related to the strain relaxation energy gain. Experimentally, we observed that CDW switching is easier at some places indicating a non negligible role of defects and the possibility of energy compensation during CDW switching. The coherent mechanism refers hereby to a simultaneous switching of the whole CDW nano domains. This cannot be initiated by a single electron. Instead, electrons tunnel elastically through the junction but dissipate their energy in the substrate. For CDW switching to occur, there must be a sufficient number of electrons dissipating their energy in a small area (on the order of a switched CDW domain, *i.e.*, $\sim$10 nm) in a short time. If dissipated electron energy is sufficient to excite a CDW frozen phonon mode to a higher

energy state, the phonon is no longer "frozen" but can move to a different ground state (*i.e.*, CDW switching occurs) after its relaxation. Since electron tunneling is a stochastic process with the number of tunneled electrons in a unit time following Poisson distribution, it seems viable that sufficient energy could be deposited on this CDW phonon mode if its relaxation time $< t >$ is long enough. Acoustic phonons, due to their lower energies, typically have longer phonon lifetimes. For example, acoustic phonon lifetimes in Si and GaAs are $\sim$1 $\mu$s[21,22] near the zone center. Note that additional electron energy transfer process (*i. e.* scattering, anharmonic interactions, electron-phonon coupling, hot electron relaxations) may also occur and compete with the CDW switching mechanism when the current increases, leading to non trivial dependence of the switching yield with the average current. It might be also possible that both incoherent and coherent processes contribute. Further studies on the mechanisms of CDW switching, a prototype of electronic phase switching change, are required to obtain a complete picture of the mechanism.

In conclusion, we reported triggering multi-mode and reversible switching of CDW in monolayer $VTe_2$ by means of STM tip pulses. The CDW multi-mode switching is found to occur between two CDW phases, $(4 \times 4)$ and $(4 \times 1)$, three orientations of the $(4 \times 1)$ phase and lastly for the $(4 \times 1)$ CDW $\pi/2$ phase slips. The CDW switching domain is spatially extensive and can reach more than 10 nm in size. The analysis of tunneling telegraph noises shows that the switching yield per electron exhibit a bias threshold around 1 eV independent of the voltage polarity. DFT and NEB calculations reveal that the easiest process is the rotation between two (4×1) CDW orinetations and that the most difficult corresponds to the (4×1) CDW $\pi/2$ phase slips, consistent with experimental observation. The spatially extended CDW multi-mode switching initiated by very gentle perturbative STM pulses are distinct from other reported CDW switching studies.[13,14] We discussed plausible switching mechanisms, with an emphasis on compromising the calculated high barrier energies for switching and how sufficient energy can be leveraged during the CDW switching. Our study

reveals that manipulation of CDW phases is possible and that tailoring CDW properties for possible applications may thus be envisaged.

## Supporting Information Available

Experimental details, Computational details, Calculations, High resolution images of CDW phases, Local density of states, Visualization of CDW sliding.

## Acknowledgement

We thank the French National Research Agency (ANR-20-CE09-0023 DEFINE2D project) and Taiwan MOST (111-2923-M-002-011- DEFINED2D project, and 110-2112-M-002 -040 -MY3) for support.

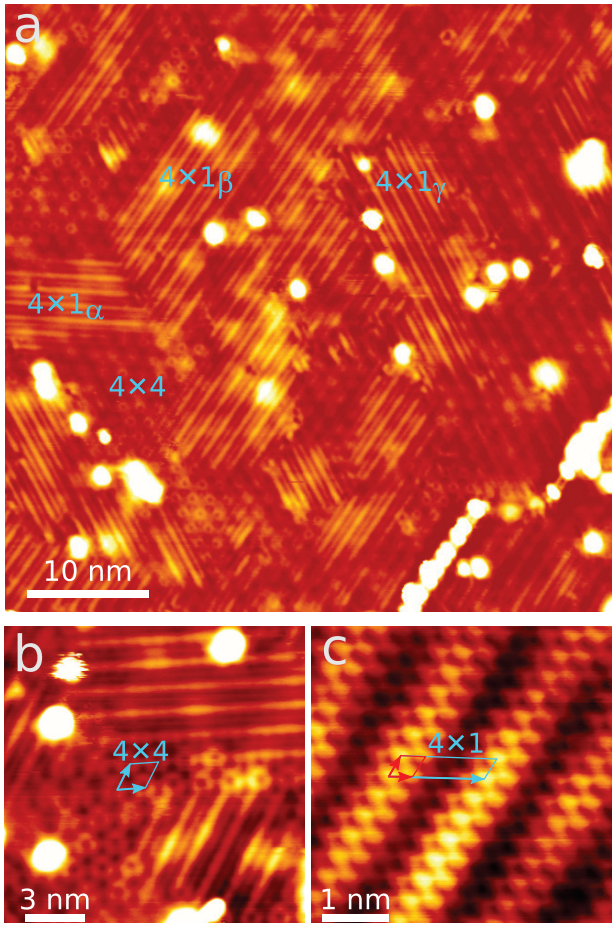


Figure 1: **(a)** STM image of a $VTe_2$ monolayer exhibiting several domains of different CDW phases. A (4×4) domain and three (4×1) (noted $4\times1_\alpha$, $(4\times1)_\beta$, $(4\times1)_\gamma$) domains aligned with the three different axes of the $VTe_2$ atomic lattice are indicated. ($V = 0.5$ V, $I = 100$ pA). **(b)** STM image showing different CDW phases and different orientations of the 4×1 phase. The unit cell vectors of the (4×4) domain with a length of 1.45 nm are indicated ($V = 0.15$ V, $I = 20$ pA). **(c)** STM atomically resolved image of the (4×1) CDW phase, the atomic and CDW unit cell vectors are indicated in red and blue respectively. The length of the atomic lattice vectors is 0.36 nm.

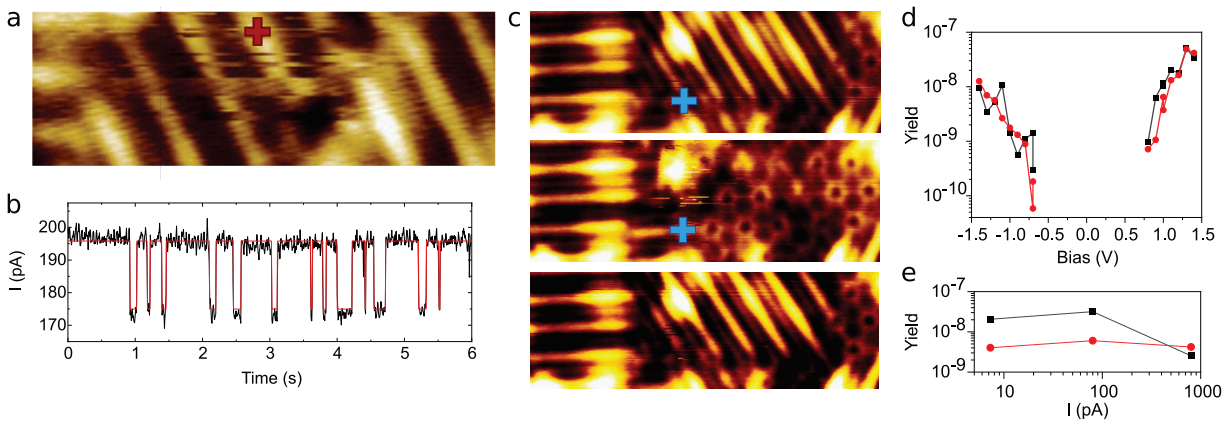


Figure 2: **(a)** STM topographic image of the fuzzy area with a defect nearby ( V = 0.8V, I = 200 pA, 10×3 $nm^2$, T = 4K ). **(b)** Tunneling current with two levels of current at (black) and its numerical fit (red) taken at the red cross in **(a)**. **(c)** Sequence of STM images showing the reversible switching of a CDW phase of $VTe_2$ monolayer. The central part exhibits a (4×1) phase (top), switches to (4×4) (middle), and finally switches back to (4×1) (bottom). The switch is activated by a voltage pulse at the tip location indicated by the blue cross (V = 0.5V, I = 100 pA, 15×5 $nm^2$). **(d)** Plot of the mean yield for the low current level (black) and the high current level (red) as a function of the bias performed with the tip position at the red cross in **(a)**. **(e)** Plot of the mean yield as a function of low level current value for the low current level (black) and high current level (red) of the telegraph signal.

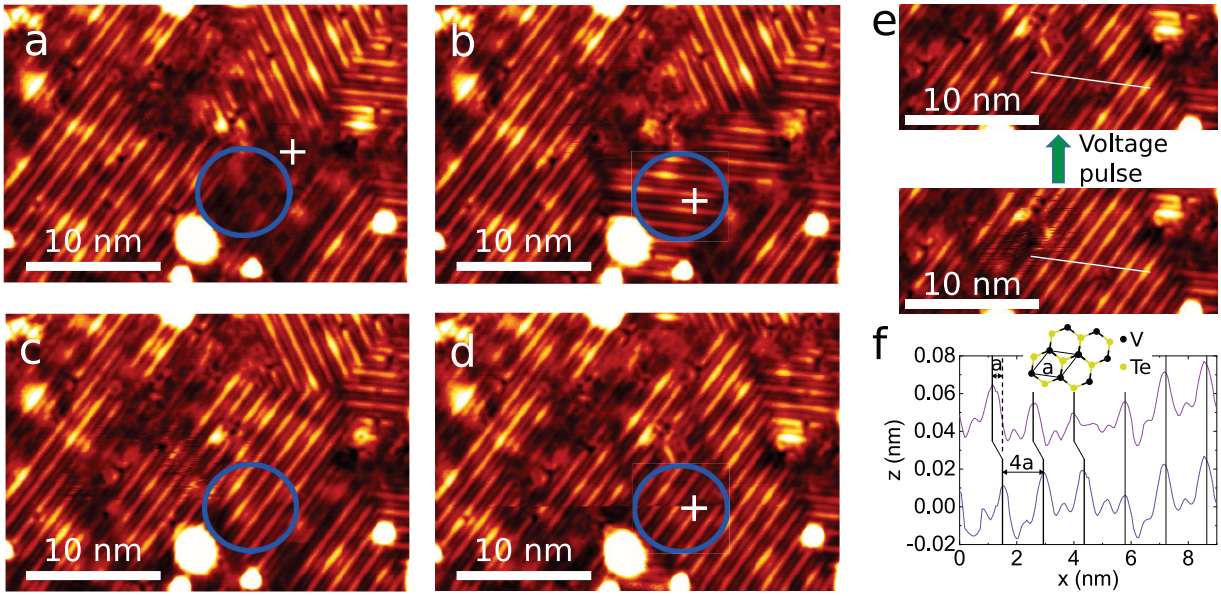


Figure 3: **(a-d)** STM topographic images of $VTe_2$ monolayer, showing a switching sequence where the area indicated by the blue circle undergoes various types of CDW change ( V = 0.5V, I = 100 pA, T = 4K, 30×20 $nm^2$). The crosses indicate the tip location used to induce a change of CDW. In **(a)** and **(b)** the voltage was applied after recording the topographic image. In **(a)** the switch occurred during a voltage sweep from -2 V to 2 V. In **(b)** a voltage pulse of -1.5 V was applied. In **(d)** a voltage pulse of 2 V was applied during the acquisition of the image. The discontinuity observed in the image reveals the CDW change that appears just after the voltage pulse **(e)** Images before and after the voltage pulse applied during image **(d)**. **(f)** Linescan measured on the bottom image of **(e)** (violet) and the top image of **(e)** (pink) along the line indicated by the white lines in **(e)**. The vertical solid lines indicate the position of the maxima of the CDW of image **(e)**.

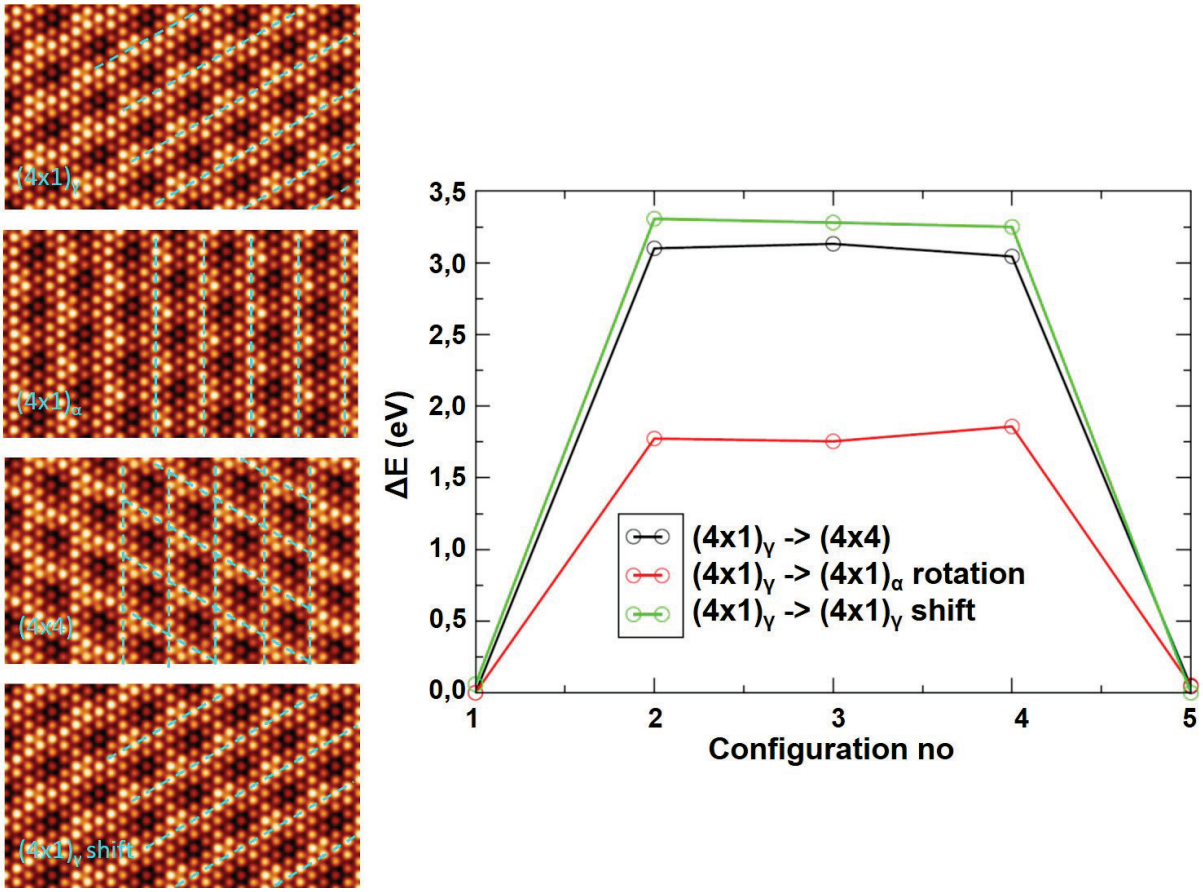


Figure 4: Calculated STM images of 9.3 × 5.4 nm$^2$ for the $(4\times1)_\gamma$, $(4\times1)_\alpha$, $(4\times4)$ CDWs of $VTe_2$ and for the $(4\times1)_\gamma$ CDW shifted by one atomic lattice distance to the left. The phase orientations are indicated in dashed cyan lines. DFT calculations of the energy barrier for the transition between these four configurations of the CDWs.

# References


(1) Rossnagel, K. On the origin of charge-density waves in select layered transition-metal dichalcogenides. *J. Phys. : Condens Matter* **2011**, *23*, 213001.

(2) Zybtsev, S. G. et al. $NbS_3$: a unique quasi-one-dimensional conductor with three charge density wave transitions. *Phys. Rev. B* **2017**, *95*, 035110.

(3) Ma, X. et al. Charge Density Wave Phase Transitions in Large-Scale Few-Layer 1T-$VTe_2$ Grown by Molecular Beam Epitaxy. *ACS Appl. Mater. Interfaces* **2019**, *11*, 10729–10735.

(4) Wang, Y.; Ren, J.; Li, J.; Wang, Y.; Peng, H.; Yu, P.; Duan, W.; Zhou, S. Evidence of charge density wave with anisotropic gap in a monolayer ${\mathrm{VTe}}_{2}$ film. *Physical Review B* **2019**, *100*, 241404.

(5) Wong, P. K. J.; Zhang, W.; Zhou, J.; Bussolotti, F.; Yin, X.; Zhang, L.; N'Diaye, A. T.; Morton, S. A.; Chen, W.; Goh, J.; de Jong, M. P.; Feng, Y. P.; Wee, A. T. S. Metallic 1T Phase, 3d1 Electronic Configuration and Charge Density Wave Order in Molecular Beam Epitaxy Grown Monolayer Vanadium Ditelluride. *ACS Nano* **2019**, *13*, 12894–12900.

(6) Coelho, P. M.; Lasek, K.; Nguyen Cong, K.; Li, J.; Niu, W.; Liu, W.; Oleynik, I. I.; Batzill, M. Monolayer Modification of $VTe_2$ and Its Charge Density Wave. *The Journal of Physical Chemistry Letters* **2019**, *10*, 4987–4993.

(7) Miao, G.; Xue, S.; Li, B.; Lin, Z.; Liu, B.; Zhu, X.; Wang, W.; Guo, J. Real-space investigation of the charge density wave in $VTe_2$ monolayer with broken rotational and mirror symmetries. *Phys. Rev. B* **2020**, *101*, 035407.

(8) Liu, M.; Wu, C.; Liu, Z.; Wang, Z.; Yao, D.-X.; Zhong, D. Multimorphism and gap opening of charge-density-wave phases in monolayer $VTe_2$. *Nano Res.* **2020**, *13*, 1733–1738.

(9) Wu, Q.; Wang, Z.; Guo, Y.; Yang, F.; Gao, C. Orbital-collaborative charge density waves in monolayer $VTe_2$. *Phys. Rev. B* **2020**, *101*, 205105.

(10) Karn, A.; Chan, Y. H.; Chazarin, U.; Chen, P.; Pai, W. W. Modification of monolayer 1T- $VSe_2$ by selective deposition of vanadium and tellurium. *AIP Advances* **2022**, *12*, 035240.

(11) Zhao, W.-M.; Ding, W.; Wang, Q.-W.; Meng, Y.-X.; Zhu, L.; Jia, Z.-Y.; Zhu, W.; Li, S.-C. Observation of Electronic Strong Correlation in $VTe_2$-$2\sqrt{3} \times 2\sqrt{3}$ Monolayer. *Phys. Rev. Lett.* **2023**, *131*, 086501.

(12) Stahl, Q.; Kusch, M.; Heinsch, F.; Garbarino, G.; Kretzschmar, N.; Hanff, K.; Rossnagel, K.; Geck, J.; Ritschel, T. Collapse of layer dimerization in the photo-induced hidden state of 1T-$TaS_2$. *Nat. Commun.* **2020**, *11*, 1247.

(13) Song, X. et al. Atomic-scale visualization of chiral charge density wave superlattices and their reversible switching. *Nat. Commun.* **2022**, *13*, 1843.

(14) Bischoff, F.; Auwärter, W.; Barth, J. V.; Schiffrin, A.; Fuhrer, M.; Weber, B. Nanoscale Phase Engineering of Niobium Diselenide. *Chem. Mater.* **2017**, *29*, 9907–9914.

(15) Chazarin, U.; Lezoualc'h, M.; Chou, J.-P.; Pai, W. W.; Karn, A.; Sankar, R.; Chacon, C. C.; Girard, Y.; Repain, V.; Bellec, A.; Rousset, S.; Smogunov, A.; Dappe, Y. J.; Lagoute, J. Formation of Monolayer Charge Density Waves and Anomalous Edge Doping in Na Doped Bulk $VSe_2$. *Adv. Mater. Interfaces* **2022**, *10*, 2201680.

(16) Pai, W. W.; Reutt-Robey, J. E. Formation of (n×1)-O/Ag(110) overlayers and the role of step-edge atoms. *Phys. Rev. B* **1996**, *53*, 15997–16005.

(17) Harsh, R.; Joucken, F.; Chacon, C.; Repain, V.; Girard, Y.; Bellec, A.; Rousset, S.; Sporken, R.; Smogunov, A.; Dappe, Y. J.; Lagoute, J. Controlling Hydrogen-Transfer Rate in Molecules on Graphene by Tunable Molecular Orbital Levels. *J. Phys. Chem. Lett.* **2019**, *10*, 6897–6903.

(18) Giustino, F. Electron-phonon interactions from first principles. *Reviews of Modern Physics* **2017**, *89*, 1–68.

(19) González, C.; Abad, E.; Dappe, Y. J.; Cuevas, J. C. Theoretical study of carbon-based tips for scanning tunnelling microscopy. *Nanotechnology* **2016**, *27*, 105201.

(20) Sheppard, D.; Xiao, P.; Chemelewski, W.; Johnson, D. D.; Henkelman, G. A generalized solid-state nudged elastic band method. *J. Chem. Phys.* **2012**, *136*, 074103.

(21) Esfarjani, K.; Chen, G.; Stokes, H. T. Heat transport in silicon from first-principles calculations. *Phys. Rev. B* **2011**, *84*, 085204.

(22) Luo, T.; Garg, J.; Shiomi, J.; Esfarjani, K.; Chen, G. Gallium arsenide thermal conductivity and optical phonon relaxation times from first-principles calculations. *Europhys. Lett.* **2013**, *101*, 16001.

# TOC Graphic

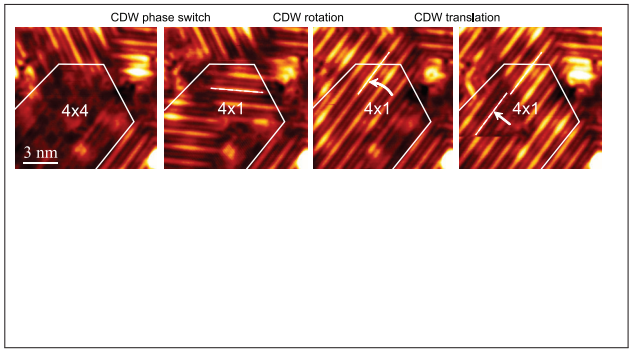
CDW phase switch
CDW rotation
CDW translation
4x4
3 nm
4x1
4x1
4x1